https://doi.org/10.1016/j.apsusc.2019.05.309

Effect of pH value and preparation temperature on the formation of magnesium phosphate conversion coatings on AZ31 magnesium alloy

Wei Zai[a,b], Yingchao Su[a], H.C. Man[b], Jianshe Lian[a] Guangyu Li[a,*]

[a] Key Laboratory of Automobile Materials, Ministry of Education, College of Materials Science and Engineering, Jilin University, Changchun 130025, China

[b] Department of Industrial & Systems Engineering, The Hong Kong Polytechnic University, Hong Kong, China

Abstract

Magnesium phosphate (Mg-P) conversion coatings were prepared on AZ31 magnesium (Mg) alloy to improve its corrosion resistance. The effect of pH value (2.5, 3.0, 3.5 and 4.0) and preparation temperature (40°C, 60°C and 80°C) on the formation of conversion coatings was investigated in this study. The formation mechanism of Mg-P conversion coating is first proposed and investigated by predominance area diagram of Mg phosphates. The morphologies, compositions and cross-section morphologies of coated samples were analyzed by scanning-electron microscopy (SEM), energy-dispersive spectrometry (EDS), X-ray photoelectron spectroscopy (XPS) and X-ray diffractometry (XRD). Electrochemical impedance spectroscopy (EIS) and potentiodynamic polarization (PDP) measurements were conducted to evaluate the short-term corrosion resistance of coated samples in Hanks' solution at 37°C and pH 7.4. In

* Corresponding author. E-mail address: guangyu@jlu.edu.cn (G. Li).

addition, a 5-day immersion test was carried out to evaluate their long-term corrosion resistance. It was found that temperature affected the corrosion performance of coated samples more significantly than pH value, and the coating formed at 80°C-pH 3.0 offered the best corrosion resistance in Hanks' solution at 37°C and pH 7.4. The formation mechanism of Mg-P coating was elucidated with reference to the pH value and Mg^{2+} ion concentration at different regions in the conversion solution according to the predominance area of magnesium phosphates. The microstructure of conversion coating suggests that it consisted of a precipitated outer layer and an *in-situ* grown inner layer. Compared with the crystallized outer layer, the dense inner layer contributed more to the corrosion resistance of the coated samples in Hanks' solution. Moreover, the corrosion mechanism of different samples including bare AZ31 Mg alloy and coated samples was discussed.

Keywords: AZ31 Magnesium alloy; Phosphate conversion coating; Corrosion resistance; Electrochemical measurements; Hydrogen evolution

1. Introduction

Since magnesium (Mg) alloy was first used as the biomaterial in 1878 [1], the potential application of Mg alloys as biomaterials has attracted the attention of numerous researchers due to their excellent cell biocompatibility and biomechanical compatibility. Mg-based biomaterial, as a promising candidate for degradable biomaterial, has a density (approximately 1.7-2.04 g/cm^3) similar to that of human cortical bone (1.8-2.1 g/cm^3) [1,2]. The elastic modulus of Mg alloys (41-45 GPa) is much closer to that of human cortical bone (3-20 GPa) compared with conventional orthopedic implant alloys such as stainless steels (190 GPa), cobalt-chromium alloys (200-300 GPa) and titanium alloys (110-116 GPa) [3]. This can effectively reduce the occurrence of the stress shielding [1,2,4,5] and stimulate the injured bony tissues in the healing responses [6-9]. Besides, compared with conventional alloys for bone fixation in fracture surgery, Mg-based alloys are degradable in physiological environment and can be excreted through urine, thus avoiding a second surgery to remove the implant or device [4,10-14] when bone healing is completed. [15]. In fact, as a human essential element, the recommended daily intake of Mg for a normal adult is about 300 ~ 400 mg [16]. In addition, Mg promotes bone tissue healing [17] via binding with phosphates, promoting the mineralization process of bony tissue and forming hydroxyapatite or calcium phosphate [5,18]. Despite the desirable mechanical and biological compatibility of Mg alloys as an orthopedic implant material, it is susceptible to rapid corrosion in physiological environment and this largely limits its application as implants. The rapid corrosion of Mg-based implants in the human body can cause accumulation of subcutaneous hydrogen gas (H_2), formation of subcutaneous gas cavities and separation of implants and tissue [11,19,20], which can directly result in surgery failure [21,22]. Alkalization, which always accompanies the

hydrogen evolution reaction, may cause alkaline poisoning if the pH value of the tissue microenvironment exceeds 7.8 [11]. Moreover, the rapid corrosion of Mg alloys not only results in hydrogen gas and alkalization but also rapidly decreases the mechanical strength of the implants and might untimely result in premature failure [23].

In order to increase the corrosion resistance of Mg alloys, numerous researchers have put a good deal of effort to address the issue through various approaches, such as addition of alloying elements, microstructure modification and surface modification [23-25]. Surface modification of Mg alloys for enhancing corrosion resistance includes conversion coating [26-29], micro-arc oxidation (MAO) [30,31], sol-gel coating [32], physical vapor deposition (PVD) [33,34], chemical vapor deposition (CVD) [35] and polymer coating. These methods, each with its own special features, are expected to form corrosion-resistant layers and lower the corrosion rate of Mg alloys [23]. Compared with other types of coatings on Mg alloy, conversion coating is a relatively simple and effective way to improve the corrosion resistance of Mg alloy. Phosphate conversion coating as an environment-friendly surface modification technique has been reported in numerous studies, employing calcium phosphate (Ca-P) [36,37], zinc phosphate (Zn-P) [38,39], manganese phosphate (Mn-P) [40], magnesium phosphate (Mg-P), and magnesium fluoride (MgF_2) [27]. However, reports of Mg-P conversion coating on Mg alloy in the literature are mainly for non-implant applications. For example, Ishizaki et al. [41] and Phuong et al. [42] reported the corrosion behavior of magnesium phosphate coating on magnesium alloy AZ31 in 3.5 wt.% NaCl aqueous solution at room temperature, which is not for applications as implants. Thus, in the present work, fabrication of Mg-P conversion coating on AZ31 and its corrosion behavior of in Hanks' solution, which is a simulated body fluid, will be studied in detail. In addition, the effect of pH value and

temperature of the conversion coating solution on the formation behavior of phosphate coatings on Mg alloy will also be elucidated.

2. Experimental procedures

2.1. Materials and preparation

Commercial extruded AZ31Mg alloy with the composition of 3.1wt% Al, 0.9wt% Zn, 0.1wt% Mn and Mg balance was used as the substrate in this study. Rectangular sample of dimensions 15 × 15 × 5 mm were cut and mechanically polished with sandpaper from #360 to #2000 grit. All samples were ultrasonically cleaned in acetone for 5 min to remove grease and contamination on the surface before subsequent experiments. The samples were treated in phosphate conversion coating solutions for 10 min. To study the effect of pH value and temperature on the quality of phosphate coatings, four pH values (2.5, 3.0, 3.5 and 4.0) and three treatment temperatures (40 °C, 60 °C and 80 °C) were used, resulting in a total of 4 × 3 = 12 preparation conditions. The compositions of the four coating solutions were shown in Table 1.

Table 1

Compositions of the magnesium phosphate conversion coating solutions

pH	Chemical composition (mol/L)			
	H_3PO_4	$Mg(NO_3)_2$	NaOH	H_2O
2.5	0.5	0.5	Balance	Balance
3.0	0.35	0.35	Balance	Balance
3.5	0.2	0.2	Balance	Balance
4.0	0.1	0.1	Balance	Balance

2.2. Microstructural characterization and compositional analysis

The surface morphologies, cross-section morphologies and chemical compositions of the conversion coatings were studied using scanning-electron microscope (SEM, Tescan Vega3) equipped with energy-dispersive spectrometer (EDS, Oxford Instruments, UK). The surface elemental composition of the conversion coating was characterized by X-ray photoelectron spectroscopy (XPS). XPS measurement was conducted using an ESCALAB 250 xi spectrometer (Thermo Fisher, USA) with a constant 20 eV pass energy and a 45° take-off angle. The XPS spectrometer was equipped with a monochromatic Al X-ray source (1486.6 eV). The measured binding energy values were calibrated by the standard binding energy of C1s peak (248.8 eV). Quantitative XPS analysis was performed by using commercial software Advantage. The phase compositions of different conversion coatings were determined using X-ray diffraction (XRD, Rigaku Dymax, Japan) with Cu Kα (λ = 0.154178 nm) radiation at 20 mA and 40 kV. The XRD patterns of conversion coatings were collected from 2θ = 10° to 60°, with a scanning rate of 4°/min.

2.3. Thermodynamic calculations

Predominance area diagram is commonly used to determine the formulation of conversion solution [42-44]. The thermo-equilibrium predominance area diagram was obtained using software MEDUSA (Make Equilibrium Diagrams Using Sophisticated Algorithms) according to the database HYDRA (Hydro Chemical Equilibrium Constant Database). Even the predominance area diagram is established at room temperature, it is still meaningful and helpful for investigating and understanding the formation mechanism of conversion coatings [45].

Fig. 1 shows the predominance area diagram for the precipitation of Mg phosphates, which varies with pH value and the concentration of Mg^{2+} ions. In the present study, the

concentration of PO_4^{3-} ions was set at 0.5, 0.35, 0.2 and 0.1M respectively. It is obvious that the corresponding points of conversion solution concentrations were near the boundaries of $MgH_2PO_4^+$/$MgHPO_4 \cdot 3H_2O$ (s).

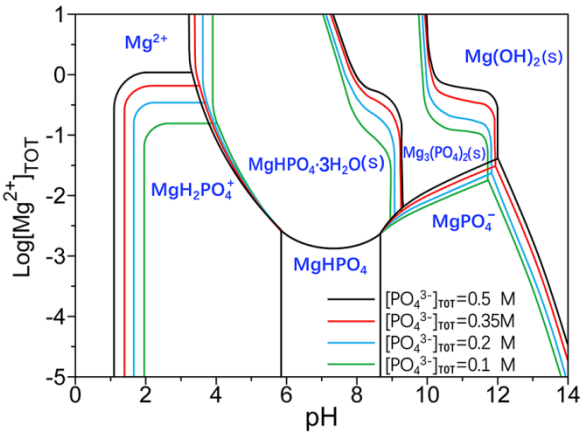

Fig. 1. Predominance area diagram for the precipitation of Mg phosphates.

2.4. Electrochemical tests

Open-circuit potential (OCP), electrochemical impedance spectroscopy (EIS) and potentiodynamic polarization (PDP) tests were conducted in Hanks' solution at pH value of 7.4±0.2 and temperature 37±0.5°C using an electrochemical station (Versa STAT3, Princeton Applied Research) in a traditional three-electrode cell. The composition of Hanks' solution is listed in Table 2 [46]. Sample with an exposed area of 1 cm^2, a platinum plate with an exposed area of 1 cm^2 and a saturated calomel electrode (SCE, E = +236 mV (vs. SHE) at T = 37±0.5°C) served as the working electrode, counter electrode and reference electrode, respectively in the cell.

Before the EIS tests and PDP tests, the samples were immersed in Hanks' solution for 30 min to reach a stable OCP. EIS measurement was carried out from 100 kHz to 10 mHz at a recording rate of 5 data-points per decade, with an AC amplitude of 10 mV at OCP. The EIS data were analyzed and fitted using software ZSimpWin. PDP test was conducted

by scanning the potential from -200 mV (vs. OCP) towards the anodic direction with the scan rate of 1 mV/s. Important corrosion parameters including the corrosion potential (E_{corr}), pitting corrosion potential (E_{pit}), ΔE ($\Delta E = E_{pit} - E_{corr}$), corrosion current density (i_{corr}), the slope of anodic branch (b_a) and the slope of cathodic branch (b_c), were extracted from the polarization curves.

Table 2

Composition of Hanks' solution.

Chemical	NaCl	KCl	$NaHCO_3$	$MgSO_4 \cdot 7H_2O$	Glucose	$CaCl_2$	KH_2PO_4	$Na_2HPO_4 \cdot 2H_2O$
Concentration (g/L)	8	0.4	0.35	0.2	1	0.14	0.06	0.06

2.5. Immersion test

Long-term immersion tests (5 days) were conducted to investigate the corrosion behaviors of all coated samples. All samples with exposed areas of 2.2 cm^2 were immersed in 300 ml of Hanks' solution at 37±0.5°C and buffered at pH = 7.4±0.2. During the immersion test, the hydrogen gas evolved from each sample was collected by a burette and the volume was recorded every 12 h. For better accuracy, 3 replicates for each type of sample were used. After the immersion test, macro morphologies of the coated samples were studied using an optical microscope.

3. Results

3.1. Coating characterization

The SEM surface morphologies of coated samples, as shown in Fig. 2, suggest that the temperature and pH value of the conversion solution significantly affected the

morphological characteristics of conversion coatings. At a fixed preparation temperature of 40°C (corresponding to micrographs in the first row of Fig. 2), the conversion coating consisted of dense flower-like columnar crystals (for solution pH = 2.5), fine equiaxial crystals (for solution pH = 3.0), dense thick plate crystals (for solution pH = 3.5) and loose thin plate crystals (for solution pH = 4.0). When the preparation temperature was elevated to 60°C (second row in Fig. 2), the conversion coating prepared at pH 2.5 consisted of short columnar crystals while the coatings prepared at pH 3.0, 3.5 and 4.0 were similar and consisted of compact equiaxial crystals. All of the conversion coatings prepared at 80°C consisted of compact equiaxial crystals at all pH values and had larger crystals compared with those prepared at 40°C and 60°C.

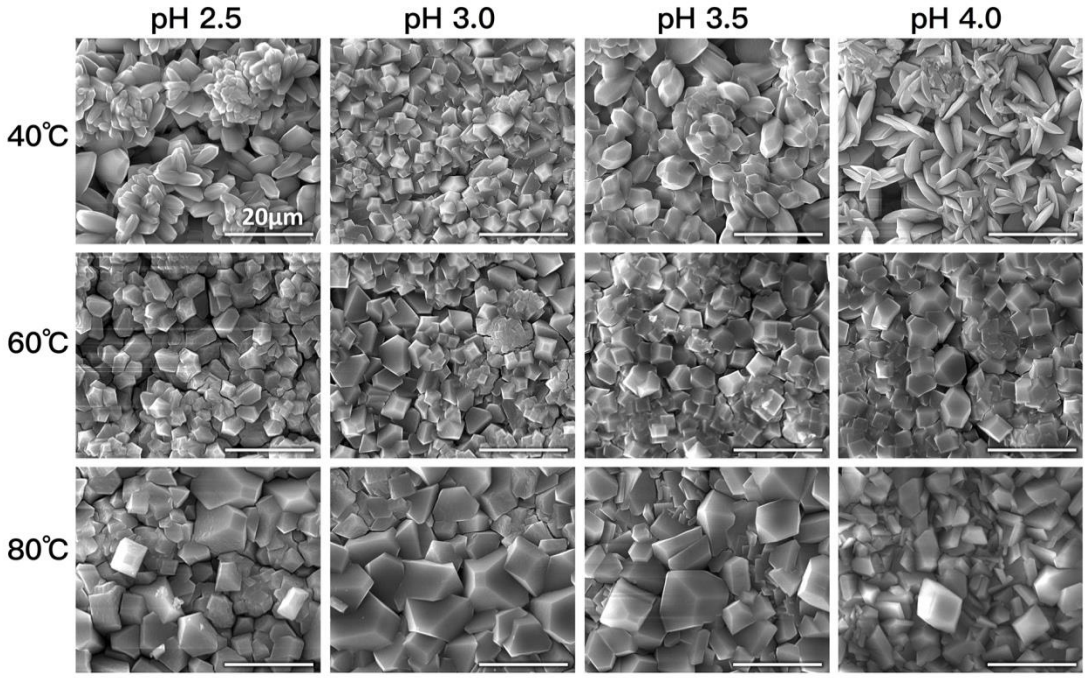

Fig. 2. SEM surface morphologies of coated samples prepared at 40°C, 60°C and 80°C in conversion solution with different pH values (2.5, 3.0, 3.5 and 4.0) (Scale bar is 20 μm).

The cross-section morphologies and the thickness of coatings prepared at different combinations of temperature and pH values are shown in Fig. 3. The thickness of coatings prepared at 40°C was about 14 ~ 15 μm. When the preparation temperature was increased to 60°C, the thicknesses of conversion coatings increased to about 22 ~ 27 μm. Coatings prepared at 80°C were thicker, with thicknesses ranging from 32 μm to 41 μm. This indicates that elevating the preparation temperature is an effective way to increase the thickness.

Comparing the surface morphologies (Fig. 2) and cross-section morphologies (Fig. 3), it can be concluded that both the pH value and temperature affect the morphologies of conversion coatings directly. At low temperature (40°C), with the increase of pH value (corresponding to decreased concentrations of $Mg^{2+}$and PO_4^{3-}), conversion coatings changed from dense columnar crystals to loose and thin plate-crystals, indicating that the pH value and ions concentration played crucial roles in influencing crystal morphology. With the increase of preparation temperature, the effect of pH value and ions concentration on the surface crystal morphology was reduced, suggesting that the preparation temperature directly determined the thickness of conversion coatings.

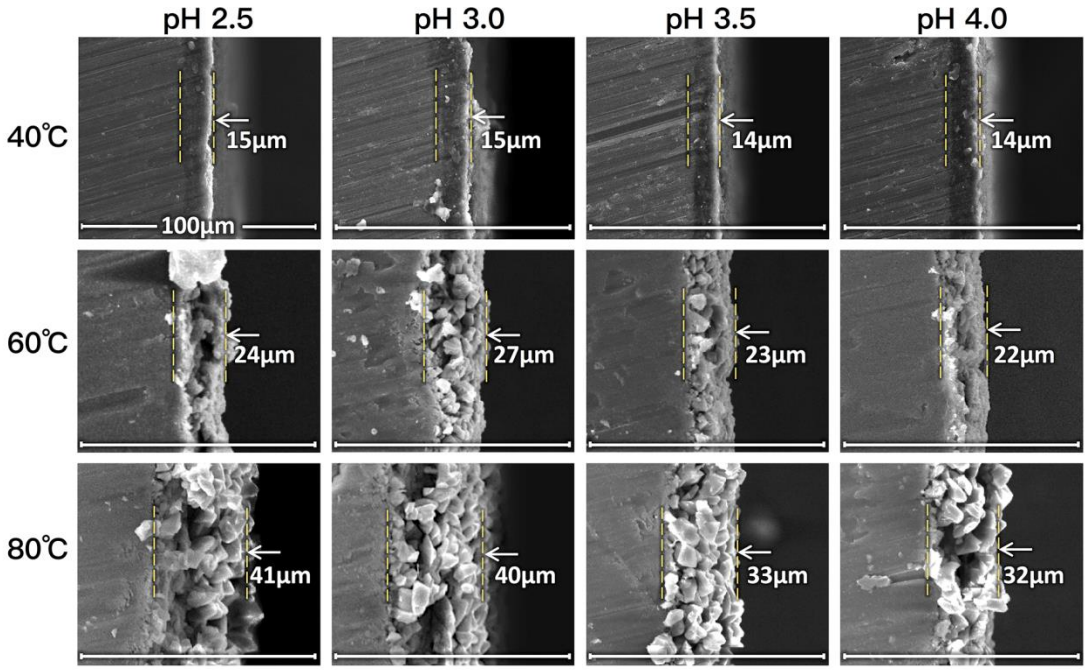

Fig. 3. Cross-section morphologies of coated samples (Scale bar is 100 μm.)

3.2. Coating composition

The EDS results for the surface compositions of conversion coatings prepared at 40°C and different pH values are shown in Fig. 4. It is clear that the compositions of coatings were similar within experimental errors. Through comparison of the proportional relationship of element Mg, P and O, it can be concluded that the ratio of Mg/P/O was about 1/1/4 and the probable main phase of conversion coatings was $MgHPO_4$.

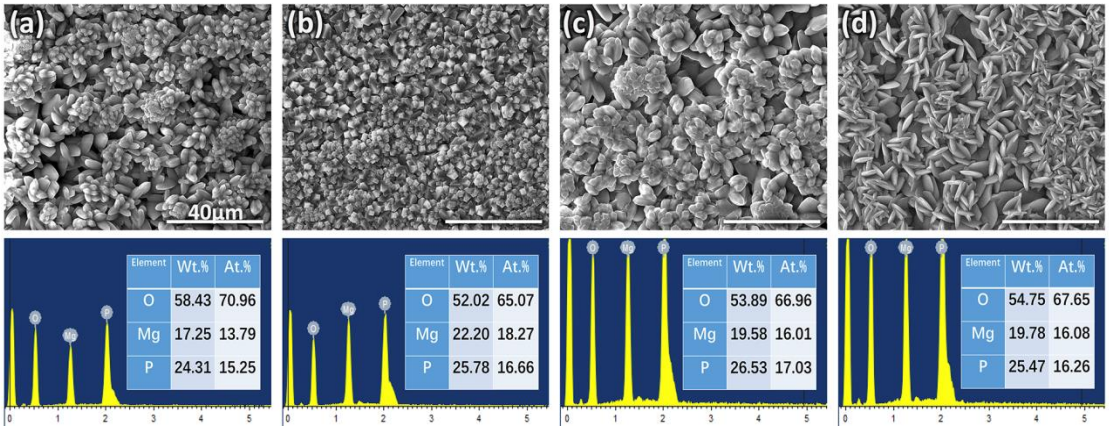

Fig. 4. EDS results and corresponding tested area of coated samples: (a) 40°C-pH 2.5, (b) 40°C-pH 3.0, (c) 40°C-pH 3.5 and (d) 40°C-pH 4.0. (Scale bar is 40 μm.)

To investigate the phase compositions of the conversion coatings, XRD analysis of coated samples prepared at 40°C and different pH values and the substrate AZ31 Mg alloy was conducted and the results are shown in Fig. 5. Distinct diffraction peaks of Mg can be observed in the XRD patterns of AZ31 Mg alloy. It is obvious that clear diffraction peaks of $MgHPO_4 \cdot 3H_2O$ appear in the XRD patterns of the conversion coatings, compared with that of Mg alloy, suggesting that the phase of $MgHPO_4 \cdot 3H_2O$ was the main component of the conversion coatings. The XRD patterns of conversion coatings prepared with different pH values are similar to each other, indicating that the compositions of conversion coatings were not affected by pH value or ions concentration under these experimental conditions.

With the increase of pH value, some changes can be observed among the XRD patterns shown in Fig. 5. It can be explained by the predominance area diagram for the precipitation of Mg phosphates given in Fig. 1. There is a band region of precipitation of $MgHPO_4 \cdot 3H_2O$ (s) corresponding to the pH value from about 3.5 to 9. Though the pH value of substrate/solution interface was slightly higher than that of the conversion solutions, except for the precipitation of $MgHPO_4 \cdot 3H_2O$, the condition at the interface did not favor the formation of other precipitations such as $Mg_3(PO_4)_2$ or $Mg(OH)_2$, since these require the pH value to reach about 9 at least.

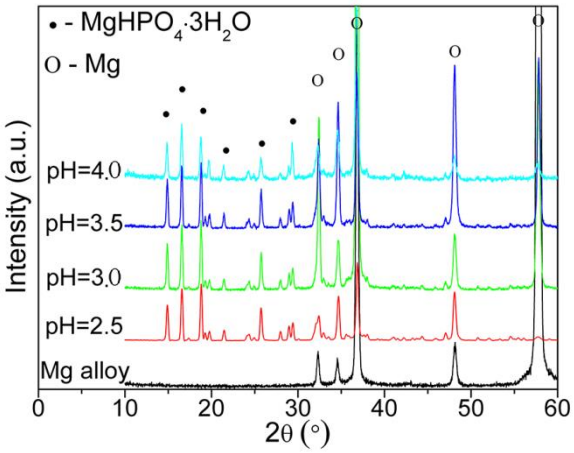

Fig. 5. The XRD patterns of substrate Mg alloy and conversion coatings prepared at 40°C.

The chemical composition and element binding stages (binding energies) of the coated sample prepared at 40°C-pH 3.0 were investigated by XPS analysis. P2p, Mg1s, O1s and the survey XPS spectra of the conversion coating are shown in Fig. 6. Mg1s, Mg2p, P2s, P2p and O2s peaks, which can be observed easily on the survey spectrum as shown in Fig. 6(a), indicate that $Mg(HPO_4)_2$, $MgHPO_4$ or $Mg_3(PO_4)_2$ may form in the conversion coating. For further investigation of the binding status, high-resolution XPS spectra of P2p, Mg1s and O1s are given in Fig. 6(b), (c), and (d). According to the possible composition of the conversion coating, all high-resolution XPS spectra were divided into several corresponding peaks through deconvolution fitting using the software Avantage.

The P2p spectrum (Fig. 6(b)) was divided into a higher peak at about 133.8 eV and a lower peak at about 134.7 eV which are assigned to the HPO_4^{2-} radical of $MgHPO_4$ and the $H_2PO_4^-$ radical of $Mg(H_2PO_4)_2$ respectively [47-50]. It is clear that element P is mainly contained in $MgHPO_4$, corresponding to the result of XRD patterns (Fig. 5). Since some residual conversion solution, which contained $Mg(H_2PO_4)_2$, remained on the surface of

conversion coating, a little amount of $Mg(H_2PO_4)_2$ was detected in the P2p spectrum. The fitting result of Mg1s spectrum shows the $MgHPO_4$ peak at about 1304.3 eV and the $Mg(H_2PO_4)_2$ peak at 1306.0 eV respectively, indicating that Mg is mainly contained in $MgHPO_4$ with a small amount in $Mg(H_2PO_4)_2$ [48,51]. The O1s spectrum, as shown in Fig. 6(d), is deconvoluted into three peaks at about 531.2, 531.9 and 533.4 eV. The peaks at about 531.2 and 531.9 eV are interpreted as oxygen in $Mg(OH)_2$ and P=O radical respectively [47,52-54]. The peak at 533.4 eV may be assigned to P-OH radical and H_2O, which is in the form of crystallization water [53]. Besides, a small peak of $Mg(OH)_2$ appears in the spectrum of O1s, while no distinct peak can be assigned to $Mg(OH)_2$ in the Mg1s spectrum. This implies that except $MgHPO_4$ and $Mg(H_2PO_4)_2$, only a very little amount of $Mg(OH)_2$ was formed on the surface of conversion coating and hard to detect. The composition of conversion coating determined from the XPS is consistent with the results of XRD analysis.

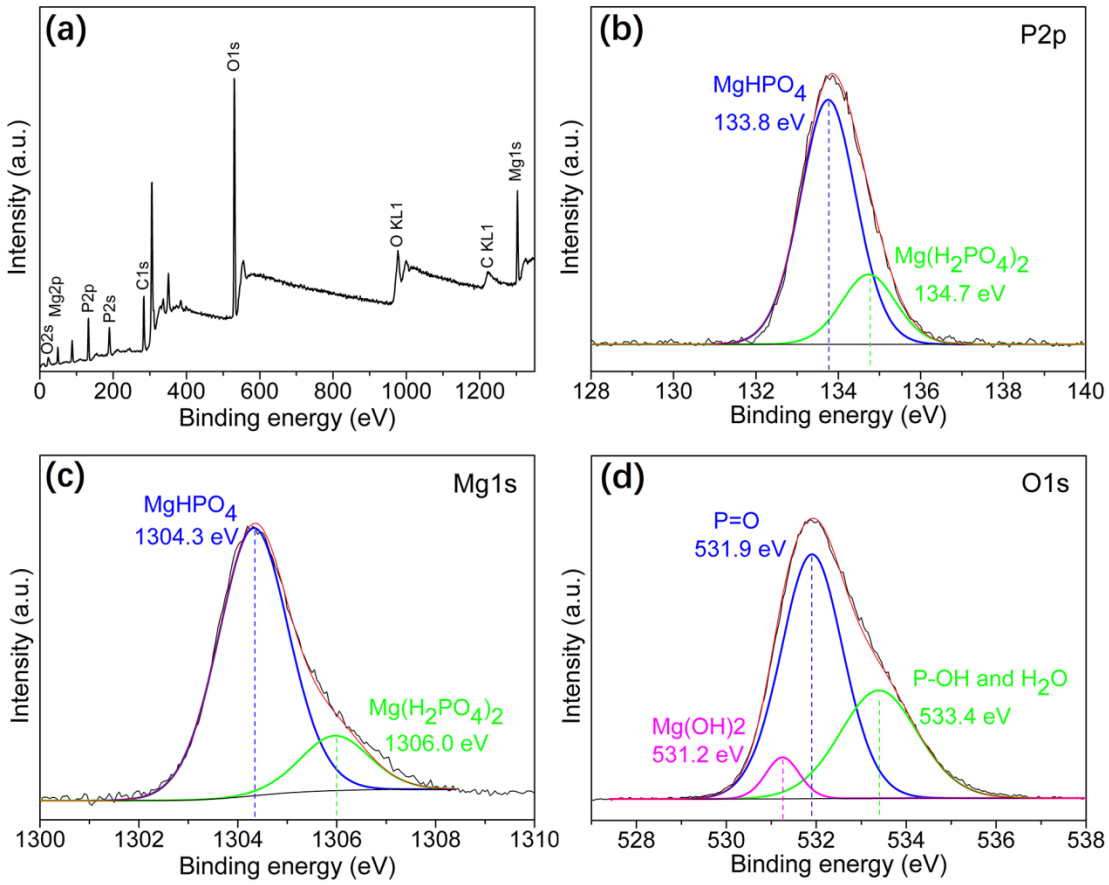

Fig. 6. XPS spectra of conversion coating on AZ31 Mg alloys (a) Survey XPS spectrum and high-resolution spectra of (b) P2p (c) Mg1s (d)O1s

3.3. Corrosion tests

3.3.1. OCP measurement

Open-circuit potential (OCP) measurement was conducted before other electrochemical tests (electrochemical impedance spectroscopy (EIS) and potential dynamic polarization (PDP) measurement), in order to ensure the tested working electrode was electrochemically stable. The immersion time of OCP test was set as 30 min and the OCP values are depicted in Fig. 7. As shown in Fig. 7(a), after about 600 s of immersion, the OCP curve of AZ31 Mg alloy stabilized at around -1.59 V. Compared

with AZ31, the stabilized OCP of other samples (40°C-pH2.5, 40°C-pH3.0, 40°C-pH3.5 and 40°C-pH4.0) were lower and varied from -1.65 V to -1.75 V. If the conversion coatings were prepared at 60°C, as shown in Fig. 7(b), the steady OCP values were in the range of -1.45V ~ -1.60V. With further increase of preparation temperature to 80°C, the steady OCP values were in the range of -1.50 V ~ -1.65 V, similar to that of samples prepared at 60°C.

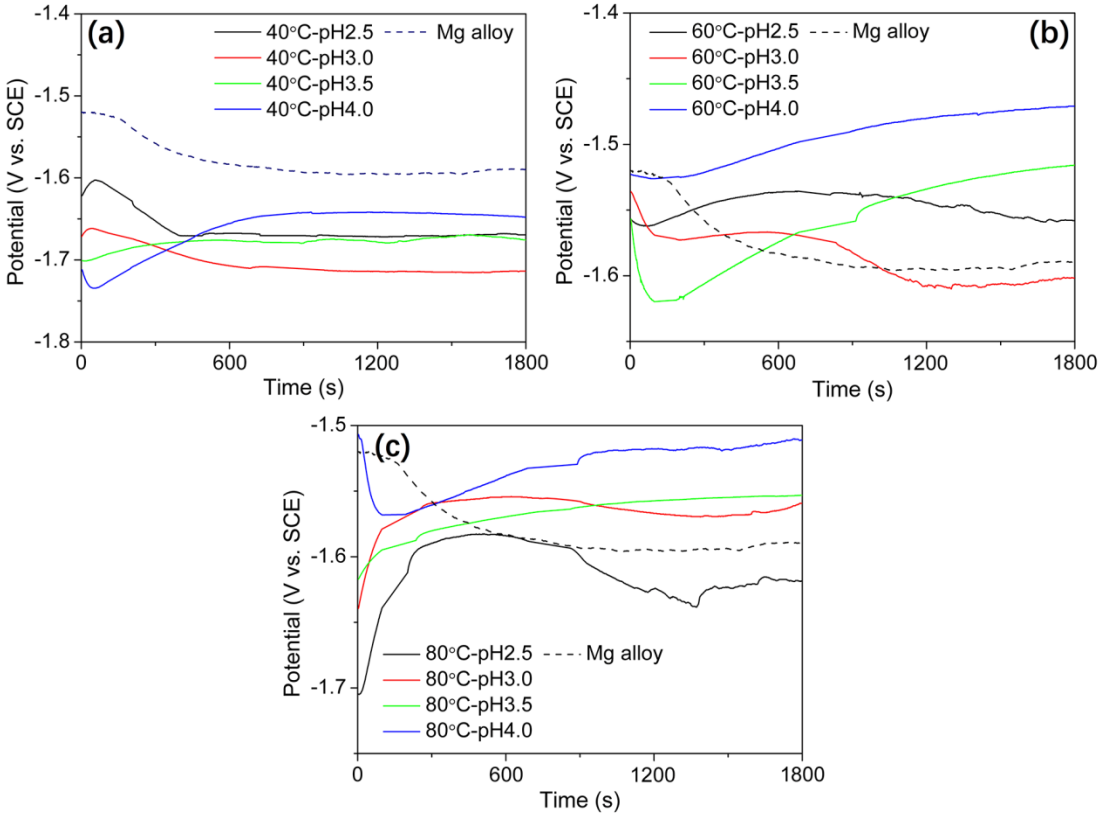

Fig. 7. OCP curves of bare and coated samples prepared at (a) 40°C (b) 60°C and (c) 80°C.

3.3.2. EIS measurement

After the OCP test, electrochemical impedance spectroscopy (EIS) measurement was conducted and the test results are presented in Fig. 8 (Nyquist plots) and Fig. 9 (Bode

plots). In order to further elucidate the corrosion characteristics and differences among samples, electrochemical equivalent circuit (EEC) models were introduced to analyze the EIS results. According to the corrosion mechanism and microstructure of uncoated and coated Mg alloy samples, two EEC models (shown in Fig. 10) were used to simulate the electrochemical processes and to fit the EIS data. The circuit description code (CDC) was introduced to represent and describe the EEC models. Because of the time-constant dispersion effect [55], a constant-phase element (CPE) was introduced to replace the capacitance (C) in EEC models and the impedance of CPE can be described as $Z_{CPE}=[Y(j2\pi f)^n]^{-1}$ (where n and Y are parameters associated with a CPE. When n = 1, Y has the unit of a capacitance). The CDCs of $R_s\ (CPE_fR_f)(CPE_{dl}R_{ct})$ and $R_s\ (CPE_{out}\ (R_{out}\ (CPE_{in}R_{in})(CPE_{dl}R_{ct})))$ represent the EEC model (a) and model (b) as shown in Fig. 10(a) and (b) respectively. In the schematic diagram of EEC (Fig. 10), R_s is solution resistance between the reference electrode and the working electrode, R_f and CPE_f are the resistance and constant phase-element pertaining to the corrosion product film (or $Mg(OH)_2$ layer) [56] on AZ31. R_{ct} is the charge transfer resistance of AZ31, CPE_{dl} is the constant phase-element of the double-layer on the interface of AZ31/electrolyte. As the $Mg(OH)_2$ layer is loose and porous, a series combination of R_s, (CPE_fR_f) and $(CPE_{dl}R_{ct})$ is used as the EEC model in (a). R_{out} and CPE_{out} are the resistance and constant phase-element of the conversion coating outer layer, while R_{in} and CPE_{in} correspond to the conversion coating inner layer.

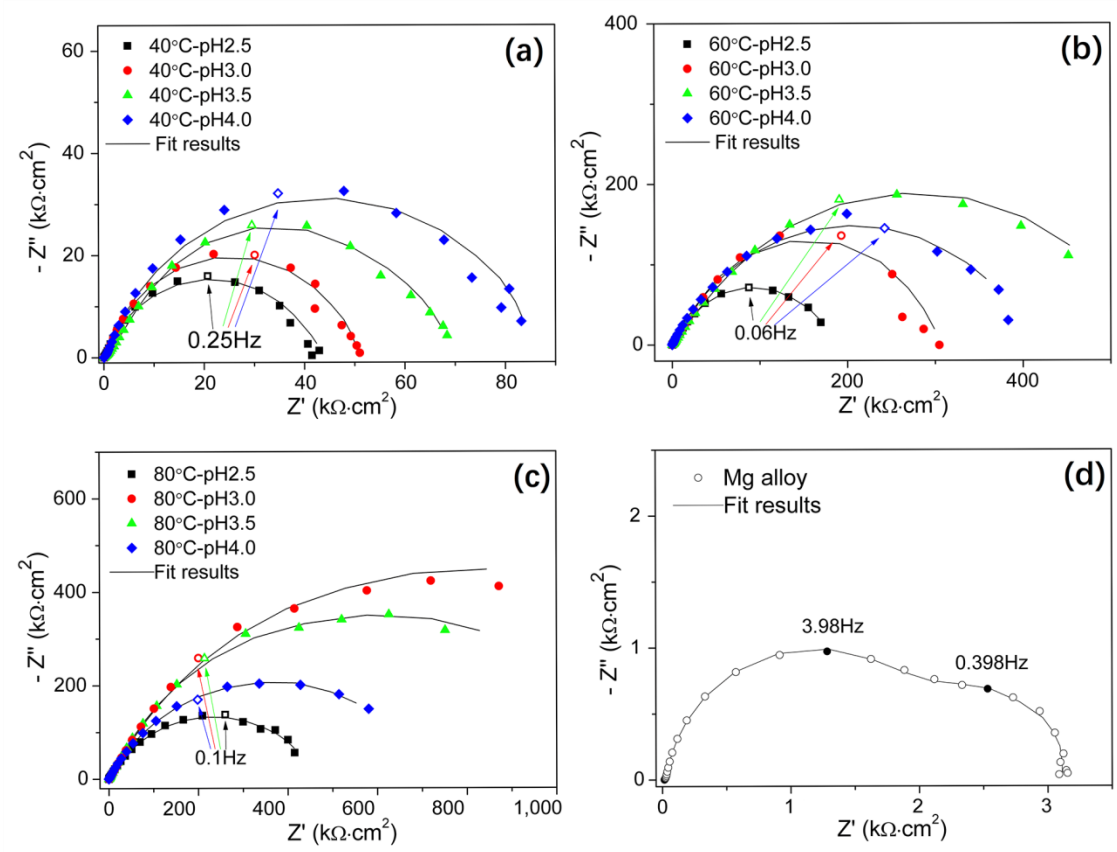

Fig. 8. Nyquist plots of coated samples prepared at (a) 40°C (b) 60°C (c) 80°C and (d) AZ31 Mg alloy

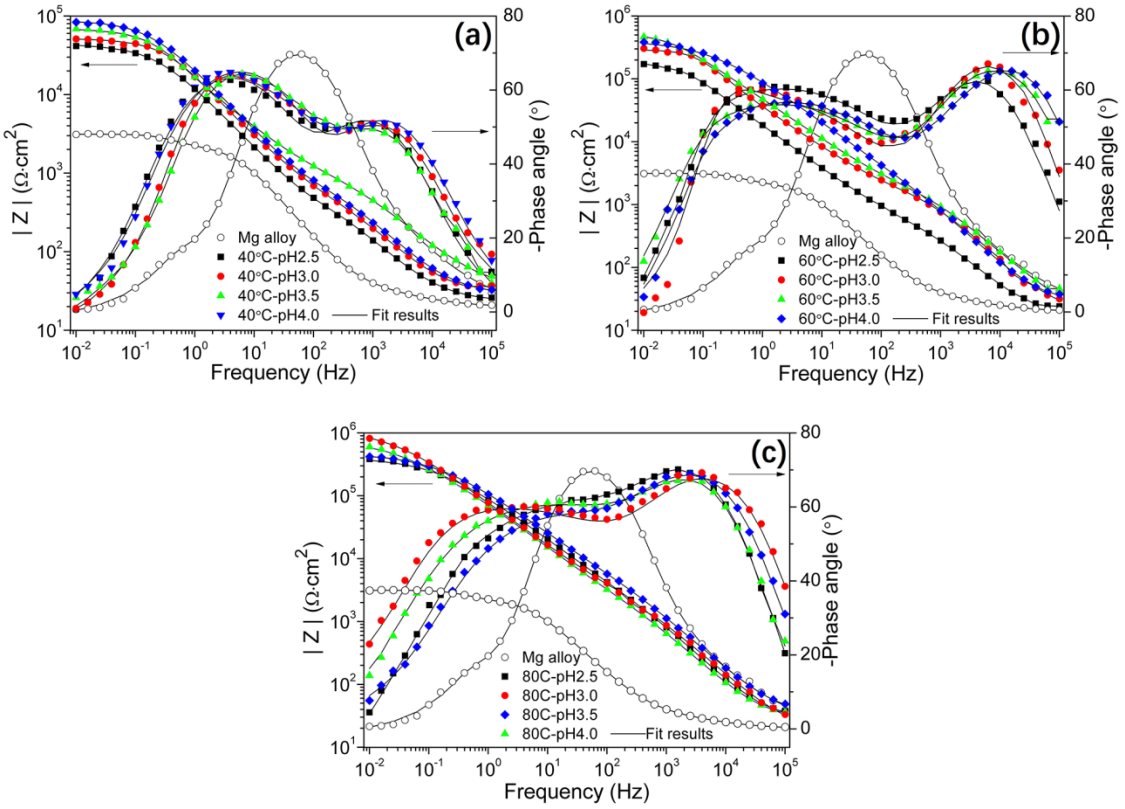

Fig. 9. Bode plots of coated samples prepared at (a) 40°C (b) 60°C (c) 80°C and AZ31 Mg alloy.

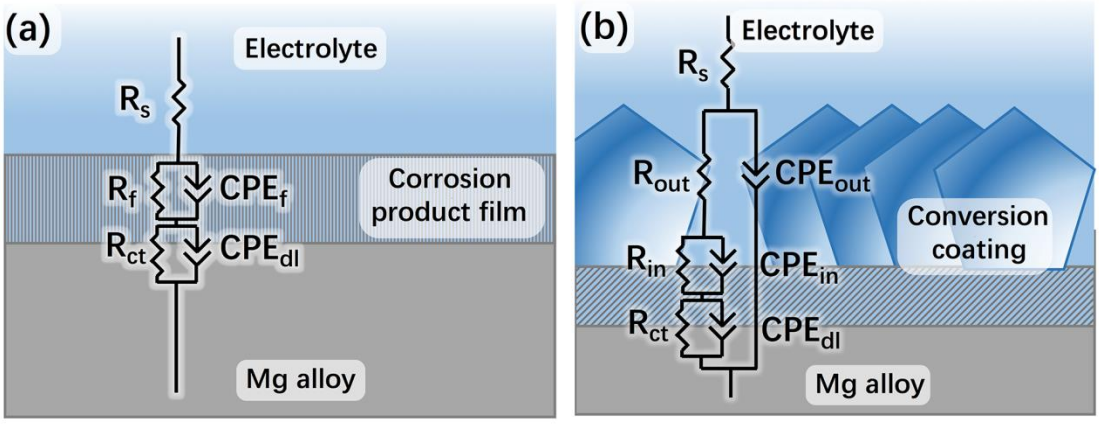

Fig. 10. EEC models of (a) AZ31 Mg alloy and (b) coated samples in Hanks' solution.

The fitting results of EIS data are listed in Table 3. In EEC model (a) and model (b), the relationships between R_p (polarization resistance) and other resistances can be described by Eqs. (1) and (2) respectively.

$$R_p = R_f + R_{ct} \quad (1)$$

$$R_p = R_{out} + R_{in} + R_{ct} \quad (2)$$

Table 3

Values of circuit elements in the EEC models from the fitting EIS data. (Units of R and Y are ($\Omega \cdot cm^2$) and ($\Omega^{-1} \cdot cm^{-2} \cdot s^n$) respectively)

		R_s	CPE_{out}		R_{out}	CPE_{in} / CPE_f		R_{in}	CPE_{dl}		R_{ct}	R_p
			Y_{out}	n_{out}		Y_{in} / Y_f	n_{in} / n_f	R_{in}	Y_{dl}	n_{dl}		
Mg alloy		20.4	---	---	---	1.91×10^{-5}	0.94	1300	1.89×10^{-4}	0.90	2038	3338
40°C	pH2.5	25.3	6.65×10^{-6}	0.79	370	1.06×10^{-5}	0.86	3.93×10^{4}	8.35×10^{-5}	0.54	1616	4.13×10^{4}
	pH3.0	35	6.17×10^{-6}	0.76	700	6.08×10^{-6}	0.97	4.23×10^{4}	2.72×10^{-5}	0.61	9663	5.26×10^{4}
	pH3.5	36.8	3.47×10^{-6}	0.71	1080	1.07×10^{-5}	0.92	5.80×10^{4}	2.33×10^{-5}	0.59	9279	6.83×10^{4}
	pH4.0	32.2	5.99×10^{-6}	0.74	830	4.73×10^{-6}	0.96	7.58×10^{4}	2.31×10^{-5}	0.61	8595	8.53×10^{4}
60°C	pH2.5	24	1.36×10^{-6}	0.88	518	1.86×10^{-5}	0.93	1.36×10^{5}	2.22×10^{-5}	0.61	4.17×10^{4}	1.79×10^{5}
	pH3.0	29.6	5.28×10^{-7}	0.86	1696	7.19×10^{-6}	1	2.46×10^{5}	1.00×10^{-5}	0.61	4.69×10^{4}	2.95×10^{5}
	pH3.5	38.2	6.05×10^{-7}	0.82	2123	9.96×10^{-6}	0.90	3.56×10^{5}	7.39×10^{-6}	0.60	1.48×10^{5}	5.06×10^{5}
	pH4.0	36	5.67×10^{-7}	0.87	3802	6.88×10^{-6}	0.87	2.25×10^{5}	2.76×10^{-6}	0.60	1.94×10^{5}	4.23×10^{5}
80°C	pH2.5	27.8	8.97×10^{-7}	0.84	3738	2.97×10^{-6}	1	4.86×10^{5}	3.09×10^{-5}	0.63	1.71×10^{5}	6.62×10^{5}
	pH3.0	32.4	7.26×10^{-7}	0.83	3656	3.32×10^{-6}	0.96	1.36×10^{6}	2.62×10^{-5}	0.62	7.55×10^{5}	2.12×10^{6}
	pH3.5	34.5	4.05×10^{-7}	0.85	2861	3.92×10^{-6}	0.86	1.19×10^{6}	1.05×10^{-5}	0.59	6.64×10^{4}	1.26×10^{6}
	pH4.0	37.6	5.35×10^{-7}	0.83	782	2.02×10^{-6}	1	4.69×10^{5}	7.55×10^{-6}	0.60	5.62×10^{4}	5.26×10^{5}

As shown in Fig. 8(d), two distinctive capacitive loops were observed in the Nyquist plot of AZ31 Mg alloy corresponding to two peaks in its Bode phase plot in Fig. 9. The first capacitive loop corresponding to the high peak in the middle-frequency range was generated by the charge-discharge process of the $(CPE_{dl}R_{ct})$ circuit, the second capacitive loop in the low-frequency range corresponds to the charge-discharge process of the (CPE_fR_f) circuit. The EIS fitting results of R_{ct} and R_f (AZ31 Mg alloy) are 2038 and 1300

$\Omega \cdot cm^2$. According to Eq. (1), R_p of AZ31 Mg alloy calculated from the EIS result is 3338 $\Omega \cdot cm^2$.

According to the Bode phase plots shown in Fig. 9(a), the samples prepared at 40°C and different pH values have two obvious peaks, including a lower peak in the high-frequency range and a higher peak in the low-frequency range. On account of the time constant of $(CPE_{dl}R_{ct})$ circuit, there is a hidden peak in the medium-frequency range. Compared with the samples prepared at 40°C, coated samples prepared at 60°C has higher peak values in the high-frequency range because of the increase of R_{out}, as shown in Fig. 9(a) and (b). With further increase of preparation temperature to 80°C, the phase angles in the medium-frequency range of Bode phase plots has an obvious increase compared with that of samples prepared at 60°C or 40°C, while there is no obvious difference in the high-frequency range compared with samples prepared at 60°C, suggesting that R_{out} of samples prepared at 60°C and 80°C have the same order of magnitude.

Comparison of the resistances R_{out}, R_{in}, R_{ct} and R_p are presented in Fig. 11. It can be observed that in all cases R_{in} is much larger than R_{out}, indicating that the compact inner layer of the conversion coating would more effectively protect the substrate from corrosion attack.

The values of R_p depend on the temperature and pH value of preparation, as is depicted in Fig. 11(d). For coated samples prepared at 40°C, R_p increases from 4.13×10^4 $\Omega \cdot cm^2$ to 8.53×10^4 $\Omega \cdot cm^2$ as the pH value increases from 2.5 to 4.0. Compared with samples prepared at 40°C, samples prepared at 60°C have higher R_p. When the preparation temperature reached 80°C, R_p increases further. The sample prepared at 80°C and pH 3.0 has the largest R_p and hence the highest corrosion resistance.

Compared with n_{in} of CPE_{in}, n_{out} of CPE_{out} are generally larger and the probable reason is that the outer layer of conversion coating is rougher and less compact than the inner layer. Moreover, n_{ct} of coated samples are less than n of CPE_{out}, CPE_{in} and CPE_{dl} of bare AZ31 Mg alloy. The dense inner layer restrains the electrochemical response of the interface of substrate/electrolyte, and therefore n_{ct} of the coated samples are less than n of other CPE.

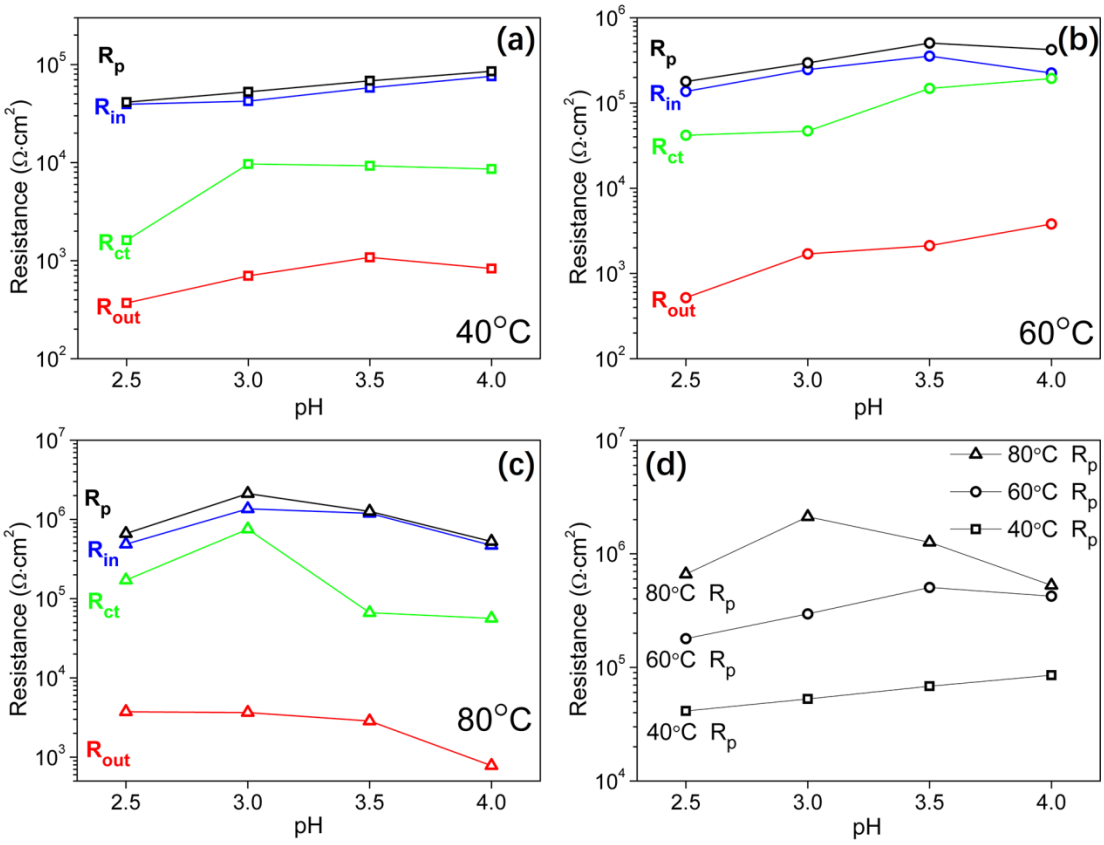

Fig. 11. Resistances comparison (R_{out}, R_{in}, R_{ct} and R_p) from EIS fitting results (Table 3) of coated samples prepared at (a) 40°C, (b) 60°C (c) 80°C and (d) comparison of R_p of all coated samples.

3.3.3. PDP measurement

Fig. 12 shows the potentiodynamic polarization (PDP) curves of all coated samples and AZ31 Mg alloy together with the Tafel slopes. Values of E_{corr}, i_{corr}, E_{pit} and ΔE (= E_{pit} - E_{corr}), b_a (slope of anodic branch line), b_c (slope of cathodic branch line) are extracted from the PDP curves and shown in Table 4. The combined effect of preparation temperature and pH value on the corrosion current density is shown in the 3D diagram in Fig. 12(d).

As shown in Fig. 12 and Table 4, i_{corr} of AZ31 Mg alloy is 6.85 μA and is larger than that of coated samples by at least an order magnitude. Among the coated samples, the one prepared under the condition 40°C-pH 2.5 has the largest i_{corr} (678 nA). With the increase of pH value from 2.5 to 4.0, i_{corr} of the coated samples prepared at 40°C decreased from 678 nA to 297 nA. When the preparation temperature was increased to 60°C, i_{corr} is found to lie in the range of 233 nA ~ 177 nA. With further increase of preparation temperature to 80°C, i_{corr} lies in the range of 171 nA ~ 57 nA and the sample prepared at 80°C-pH3.0 has the lowest i_{corr} of 57 nA.

Interestingly, for AZ31 substrates coated with Mg-P conversion coatings, their E_{pit} values are stable and lie in a narrow range of -1.40V ~ -1.43V. Compared with coated samples prepared at 60°C and 80°C, samples prepared at 40°C has a lower E_{corr} and hence enjoys a larger ΔE.

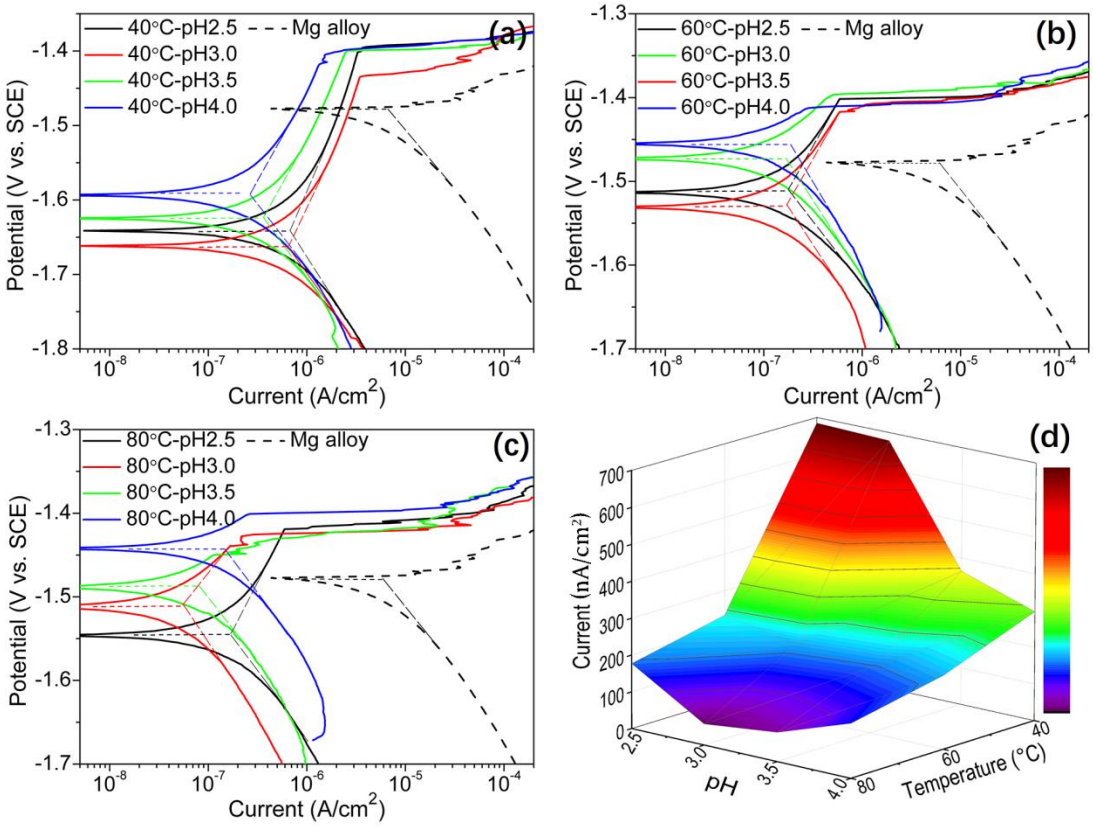

Fig. 12. PDP curves of coated samples prepared at (a) 40°C, (b) 60°C, (c) 80°C and AZ31 Mg alloy in Hanks' solution at 37°C and pH 7.4 and (d) corrosion current density at different combinations of preparation temperature and pH values.

Table 4

Corrosion parameters extracted from the PDP curves shown in Fig. 12.

	Mg	40°C				60°C				80°C			
	alloy	pH2.5	pH3.0	pH3.5	pH4.0	pH2.5	pH3.0	pH3.5	pH4.0	pH2.5	pH3.0	pH3.5	pH4.0
b_a (mV/dec)	----	305	289	232	230	213	213	----	----	240	135	----	----
$-b_c$ (mV/dec)	154	203	184	179	195	157	187	190	205	182	187	154	165
i_{corr} (nA/cm^2)	6850	683	678	364	297	220	233	177	200	171	57	79	148
E_{corr} (V vs.SCE)	147	-1.64	1.66	1.63	158	151	153	147	146	154	151	149	144
E_{pit} (V vs.SCE)	----	-1.40	1.43	140	140	140	142	140	141	142	143	143	140
ΔE (V)	----	0.24	0.23	0.23	0.18	0.11	0.11	0.07	0.05	0.12	0.08	0.06	0.04

3.3.4. Immersion test

The corrosion morphologies of coated samples after 5 days of immersion in Hanks' solution are shown in Fig. 13. Samples prepared at 40°C suffered from severe filiform corrosion and pitting corrosion. More than half of their surface area was corroded, with white precipitates forming on their surface after the immersion test. Samples prepared at 60°C had better corrosion resistance. They suffered from filiform corrosion or pitting corrosion, but to a less extent than that of samples prepared at 40°C. Compared with coated samples prepared at 40°C and 60°C, samples prepared at 80°C had the least corroded area. This reveals that the corrosion resistance of the coated samples increased with the preparation temperature.

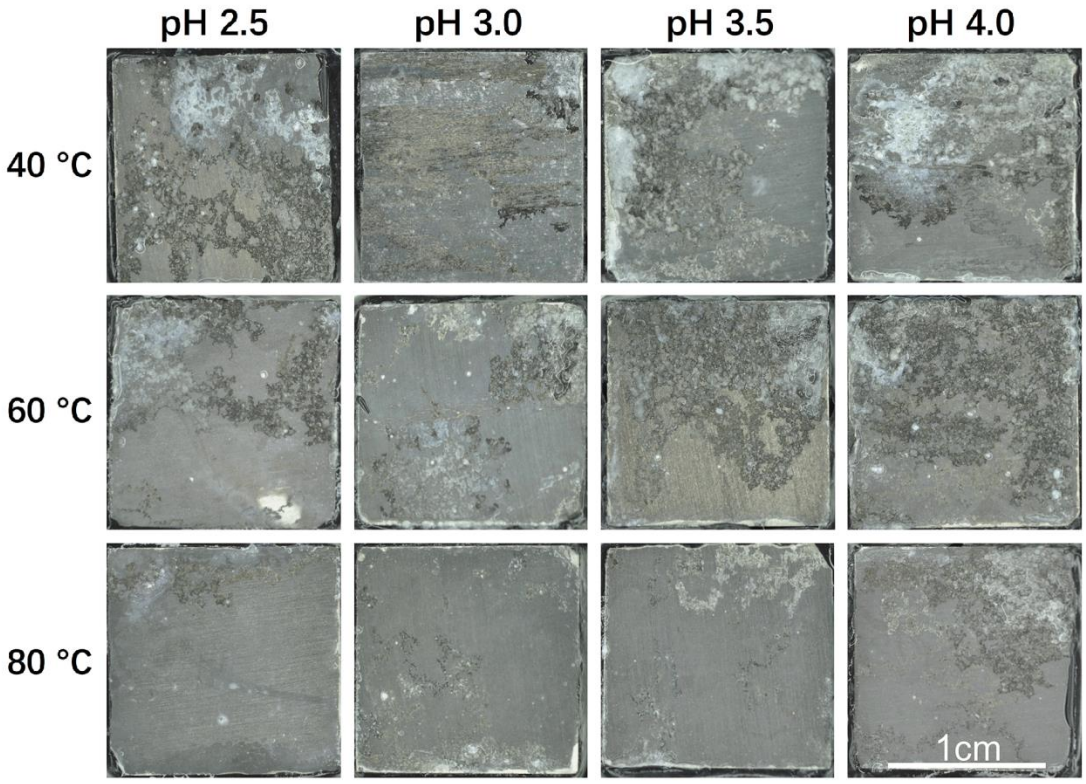

Fig. 13. Corrosion morphologies of all coated samples after the 5-day immersion test in Hanks' solution at 37°C and pH 7.4.

As 1 mol of hydrogen gas evolved corresponds to 1 mol of corroded Mg, hydrogen evolution volume is commonly used to estimate the long-term corrosion rate of Mg alloy as it is more accurate than electrochemical or gravimetric methods [11]. The cumulative volume of hydrogen evolved is plotted as a function time in Fig. 14. On the first day, the volume of hydrogen evolved from of AZ31 reached about 2±0.3 ml. In comparison, the amount of hydrogen evolved from the coated samples was much smaller or even negligible for coated samples prepared at 80°C. The total volume evolved for bare AZ31 was 6.2±0.6ml after the 5-day test, which was significantly larger than that of the coated samples. Another observation from Fig. 14 is that the effect of preparation temperature is much more significant that of the pH value. Among all types of samples, the sample prepared at 80°C and pH 3.0 yielded the smallest volume of hydrogen, meaning the smallest corrosion rate or best corrosion resistance.

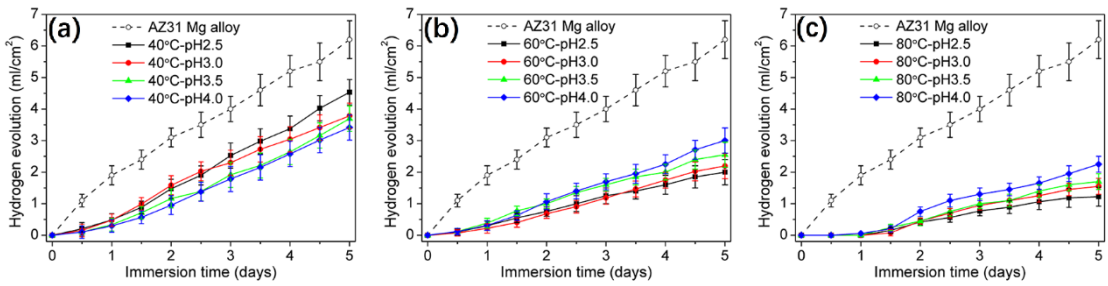

Fig. 14. Hydrogen evolution volume of AZ31 Mg alloy and coated samples prepared at (a) 40°C (b) 60°C and (c) 80°C tested in Hanks' solution at 37°C and pH 7.4.

4. Discussion

Based on the results above, the formation mechanism of the conversion coating is investigated and proposed. A schematic diagram illustrating the mechanism is depicted in Fig. 15. The formation mechanism of conversion coating consists of two main processes, including process I: the dissolution of Mg alloy substrate corresponding to Eq.

(3), and process II: the formation of conversion coating corresponding to Eq. (4). Once the Mg alloy sample is immersed in the acidic conversion solution, it reacts with the H^+ in the conversion solution and transforms into Mg^{2+} and H_2 (Eq. (3)) as depicted in Fig. 15(a), resulting in the decrease of H^+ ions concentration and the increase of the pH value nearby the substrate/solution interface corresponding to the region of Mg-P coating as shown in Fig. 15(b). On account of the dissolution of Mg which causes the accumulation of Mg^{2+} ions and the increase of pH value in the region of Mg-P coating simultaneously, there is a supersaturation of Mg^{2+} ions ($\triangle Mg^{2+}$) formed in the $MgHPO_4 \cdot 3H_2O$ predominance area corresponding to pH value *z*, as shown in Fig. 15(c) which corresponds to the intersection (Mg^{2+}, $MgH_2PO_4^+$, and $MgHPO_4$) of predominance area diagram shown in Fig. 1. Because of the supersaturation of Mg^{2+} ($\triangle Mg^{2+}$) in the $MgHPO_4 \cdot 3H_2O$ predominance area, Mg^{2+} ions and HPO_4^{2-} ions combine to form the precipitate $MgHPO_4 \cdot 3H_2O$ (Eq. (4)) on Mg alloy substrate. With the accumulation of the precipitate $MgHPO_4 \cdot 3H_2O$ in the region of Mg-P coating, conversion coating forms on the substrate and the conversion solution is separated into three regions, including Mg-P conversion coating region (corresponding to pH value $z \sim y$), diffusion zone (corresponding to pH value $y \sim x$) and conversion solution region (corresponding to pH value x) respectively, as shown in Fig. 15(b). According to the pH value and the concentration of Mg^{2+} ions, the region of Mg-P coating in Fig. 15(a) corresponds to the region of high pH value ($z \sim y$) in Fig. 15(b) and the region of $MgHPO_4 \cdot 3H_2O$ predominance area in Fig. 15(c). In the region of Mg-P coating, $MgHPO_4 \cdot 3H_2O$ forms on the Mg alloy substrate continually. Between this region and the conversion solution region is the diffusion zone (Fig. 15(a)). The diffusion zone only transfers ions and hydrogen gas between the conversion solution region and Mg-P coating region. H_2 and

Mg^{2+} ions are generated on the interface and diffuse into the conversion solution region through the diffusion zone. Meanwhile HPO_4^{2-} and H^+ ions from conversion solution region cross the diffusion zone to reach the Mg-P coating region, providing reactants for the formation of more Mg-P precipitate. It is clear that the supersaturation of Mg^{2+} plays an important role in the precipitation of Mg-P coating.

Therefore appropriate selection of the preparation temperature can effectively accelerate the reaction on the interface of substrate/solution, and the region of Mg-P coating will enlarge simultaneously, which directly increase the thickness and corrosion resistance of the Mg-P conversion coating. This is evidenced by the cross-section morphologies (Fig. 3) and the results of EIS and PDP tests. Whereas, compared with temperature, the pH value has a relatively complex influence on the formation of Mg-P coating. On the one hand, decreasing the pH value can accelerate the reaction on the interface, enlarge the region of Mg-P coating and increase the thickness of the coating. On the other hand, when the pH value is excessively low, the conversion coating may be dissolved violently nearby the region of diffusion zone, which will decrease the thickness and corrosion resistance of the Mg-P coating. When the preparation temperature was 40°C, with the decrease of pH value, the thickness of Mg-P coating was slightly increased (as shown in Fig. 3). However, its anticorrosion performance decreased dramatically (as shown in Fig. 12). When the temperature was 60°C or 80°C, a proper decrease of pH value could also improve the thickness, and at the pH of 3.5 (60°C) and 3.0 (80°C), the Mg-P coating had the optimal corrosion performance.

Process I $$Mg + 2H^+ = Mg^{2+} + H_2\,(g) \quad (3)$$

Process II $$Mg^{2+} + HPO_4^{2-} + 3H_2O = MgHPO_4 \cdot 3H_2O(s) \quad (4)$$

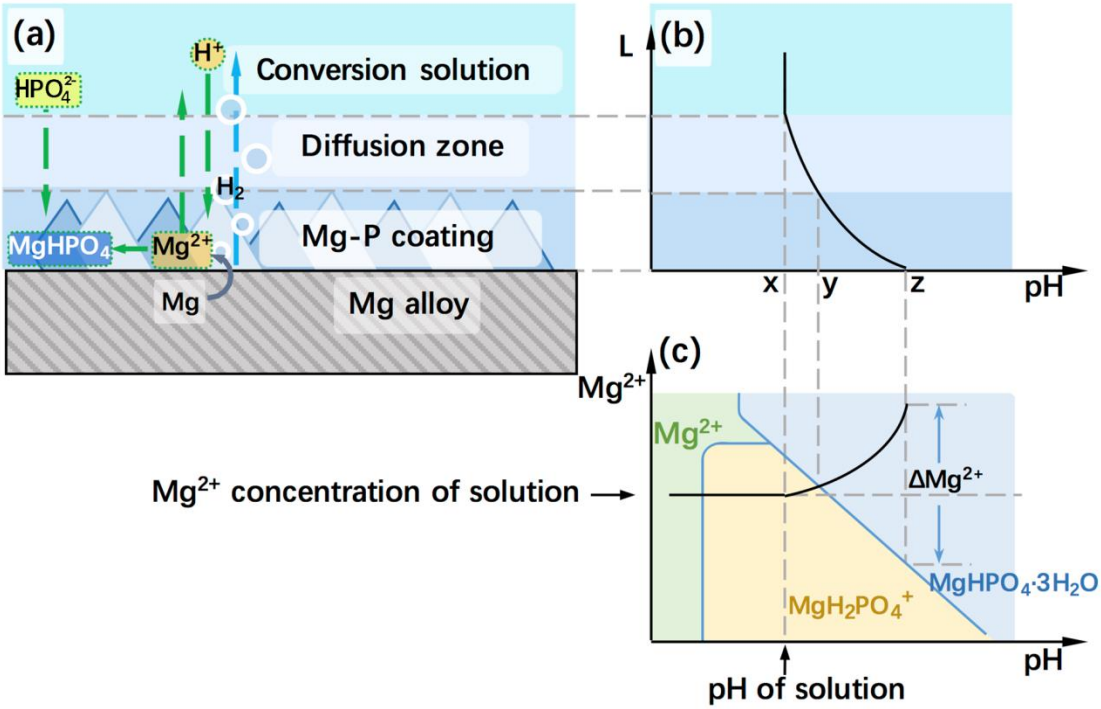

Fig. 15. Schematic diagram for the formation mechanism of conversion coating.

In order to investigate the microstructure of conversion coating, micrograph of the cross-section of sample 80°C-pH3.0 is presented in Fig. 16(a). It is easy to see that the conversion coating consists of a crystalline outer layer and smooth inner layer. Compared with the rough outer layer, the inner layer is denser and thinner. This difference in microstructure suggests that the formation mechanisms of these two layers might be different. The thicker outer layer was possibly precipitated from the conversion solution as previously mentioned (shown in Fig. 15), resulting in a rougher morphology. On the other hand, the thinner inner layer probably grew in-situ from the Mg alloy substrate via direct reaction of HPO_4^{2-} ions with Mg on the solid surface. Thus, the thin compact inner layer is the real conversion coating and it contributes to most of the corrosion resistance of the whole coating. This conclusion is supported by the much higher resistance of the inner layer than the outer layer shown in Fig. 11 and Table 3.

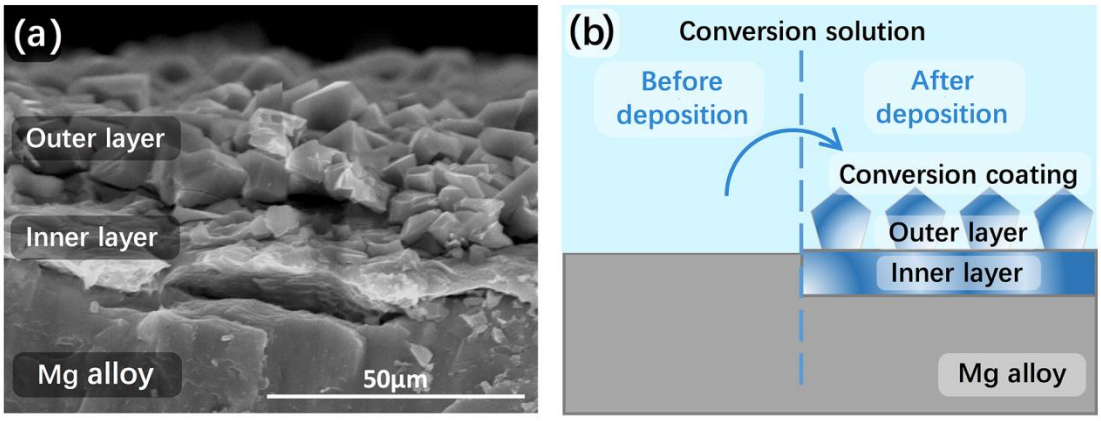

Fig. 16. (a) Feature of conversion coating (prepared at 80°C-pH3.0) which consists of the outer layer and inner layer (b) schematic diagram of the formation of conversion coating.

As shown in Fig. 12, the E_{corr} of the coated samples prepared at 60°C and 80°C is evidently higher than that of samples prepared at 40°C and similar to that of the substrate AZ31 Mg alloy. This could possibly be explained by the relationship of anodic reaction rate and cathodic reaction rate as shown in Fig. 17(a). The corrosion processes of AZ31 Mg alloy consist of an anodic reaction (Eq. (5)) and a cathodic reaction (Eq. (6)) corresponding to the anodic solid line ($I_{e,Mg}$) and the cathodic solid line ($I_{e,H2}$) respectively in the polarization diagram (Fig. 17(a)), where K_a and K_c are the Tafel slopes of the anodic and cathodic branch. Owing to the active nature of Mg, galvanic corrosion caused by the second phase β in the Mg alloy always dominates the corrosion rate of Mg alloy [57]. At the cathodic site (second phase β) the cathodic reaction (Eq. (6)) takes place and consumes the electrons generated from the anodic site (Mg matrix phase or α phase, Fig. 17(b)). Meanwhile, on the anodic site (matrix phase α), some Mg dissolves to form free Mg^{2+} ions, providing electrons to the cathodic phase β [58]. The reactions taking place in Fig. 17(b) are given below.

Anodic reaction	$Mg \rightarrow Mg^{2+} + 2e^-$	(5)
Cathodic reaction	$2H_2O + 2e^- \rightarrow 2OH^- + H_2(g)$	(6)
Overall reaction	$Mg + 2H_2O \rightarrow Mg^{2+} + 2OH^- + H_2(g)$	(7)

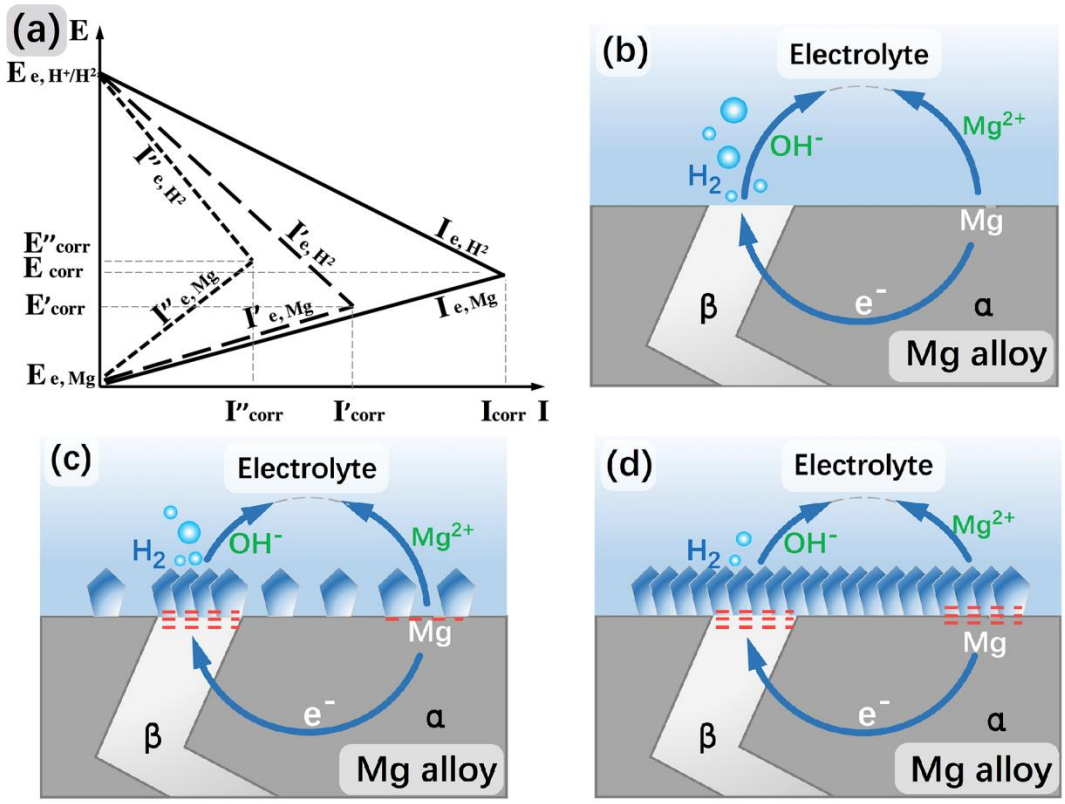

Fig. 17. (a) Polarization diagram and schematic diagrams of corrosion process in (b) AZ31 Mg alloy corresponding to that two solid lines in polarization diagram, (c) coated samples prepared at low temperature (40°C) corresponding to that two dashed lines in polarization diagram and (d) coated samples prepared at high temperature (60°C and 80°C) corresponding to that two dotted lines in polarization diagram.

It is well known that the conversion coating preferentially precipitated on the cathodic phase [43,59]. Thus, the conversion coating prepared at low temperature (40°C) is relatively thin and could not uniformly cover the anodic phase α and cathodic phase β

simultaneously. Due to the denser coating on the β phase, as shown in Fig. 17(c), the cathodic reaction is remarkably controlled by the decrease of cathodic branch slope (K_c) which is shown in Fig. 17(a) by the dashed line ($I'_{e,H2}$). As the anodic reaction was less affected, the anodic branch slope (K_a) only has a slight increment as shown in Fig. 17(a) by the dashed line ($I'_{e,Mg}$). Therefore, the intersection point of cathodic and anodic branch, that is the corrosion potential (E'_{corr}), is lower than that of AZ31 Mg alloy (E_{corr}). When the preparation temperature is increased to 60°C or 80°C, denser and thicker conversion coatings form on the Mg alloy substrates as shown in the surface morphologies (Fig. 2) and cross-section morphologies (Fig. 3). The denser conversion coating more effectively protects cathodic phase β and anodic phase α from corrosion at the same time. Therefore the cathodic reaction and anodic reaction are reduced simultaneously (Fig. 17(a)) as represented by the dotted line. Owing to the similar increment of $-K_c$ and K_a, the E''_{corr} of coated samples prepared at high temperature (60°C or 80°C) is close to that of AZ31 Mg alloy and higher than that of coated samples prepared at low temperature (40°C), which is coincident with the PDP test results as shown in Fig. 12 and Table 4.

5. Conclusions

The following conclusions can be drawn from this study.

1. Mg-P conversion coatings were prepared under different conditions at different pH values and temperatures. Based on the results of XRD, EDS and XPS analysis, it can be concluded that the main phase of the conversion coatings prepared in this work was $MgHPO_4 \cdot 3H_2O$.

2. Compared with the pH value, the preparation temperature affects the thickness of coating and improves its corrosion resistance more significantly. Among the samples prepared at different temperatures, the samples prepared at 80°C had a thicker coating and a higher corrosion resistance, and the sample prepared under the condition of 80°C-pH 3.0 had the highest corrosion resistance.

3. The microstructure of conversion coating suggests that the coating consisted of a precipitated outer layer and an *in-situ* grown inner layer. Compared with the crystalline outer layer, the inner layer contributed more to the overall polarization resistance, indicating that the inner layer played a vital role in the corrosion performances of coated samples in Hanks' solution.

4. Through the exploration of Mg-P conversion coating formation mechanism, it is concluded that appropriate pH value and higher temperature can accelerate the formation of Mg-P coating.

Acknowledgements

The work described in this paper was supported by the National Natural Science Foundation of China (Grant No. 31070841, 51705195), China Postdoctoral Science Foundation (Grant No. 801161082418) and a Research Grant (Project No. G-YBF2) from The Hong Kong Polytechnic University. Support from the infrastructure of the University is also acknowledged.

References

[1] F. Witte, Reprint of: The history of biodegradable magnesium implants: A review, Acta Biomater. 23 (2015) S28–S40. doi:10.1016/j.actbio.2015.07.017.

[2] F. Witte, J. Fischer, J. Nellesen, H.A. Crostack, V. Kaese, A. Pisch, F. Beckmann, H. Windhagen, In vitro and in vivo corrosion measurements of magnesium alloys, Biomaterials. 27 (2006) 1013–1018. doi:10.1016/j.biomaterials.2005.07.037.

[3] V.P. Mantripragada, B. Lecka-Czernik, N.A. Ebraheim, A.C. Jayasuriya, An overview of recent advances in designing orthopedic and craniofacial implants, J. Biomed. Mater. Res. - Part A. 101 (2013) 3349–3364. doi:10.1002/jbm.a.34605.

[4] M.P. Staiger, A.M. Pietak, J. Huadmai, G. Dias, Magnesium and its alloys as orthopedic biomaterials: A review, Biomaterials. 27 (2006) 1728–1734. doi:10.1016/j.biomaterials.2005.10.003.

[5] R. Zeng, W. Dietzel, F. Witte, N. Hort, C. Blawert, Progress and challenge for magnesium alloys as biomaterials, Adv. Eng. Mater. 10 (2008) 3–14. doi:10.1002/adem.200800035.

[6] L. Rodrigues, Inhibition of Bacterial Adhesion on Medical Devices, in: Bact. Adhes., 2011: pp. 351–367. doi:10.1007/978-94-007-0940-9.

[7] D. Bellucci, V. Cannillo, A. Cattini, A. Sola, A new generation of scaffolds for bone tissue engineering, Ind. Ceram. 31 (2011).

[8] A.R. Boccaccini, J.J. Blaker, Bioactive composite materials for tissue engineering scaffolds, Expert Rev. Med. Devices. 2 (2005) 303–317. doi:10.1586/17434440.2.3.303.

[9] V. Mouriño, A.R. Boccaccini, Bone tissue engineering therapeutics: controlled drug delivery in three-dimensional scaffolds., J. R. Soc. Interface. 7 (2010) 209–27. doi:10.1098/rsif.2009.0379.

[10] C. Castellani, R.A. Lindtner, P. Hausbrandt, E. Tschegg, S.E. Stanzl-Tschegg, G. Zanoni, S. Beck, A.M. Weinberg, Bone-implant interface strength and osseointegration: Biodegradable magnesium alloy versus standard titanium control, Acta Biomater. 7 (2011) 432–440. doi:10.1016/j.actbio.2010.08.020.

[11] G. Song, Control of biodegradation of biocompatable magnesium alloys, Corros. Sci. 49 (2007) 1696–1701. doi:10.1016/j.corsci.2007.01.001.

[12] S. Shadanbaz, G.J. Dias, Calcium phosphate coatings on magnesium alloys for biomedical applications: A review, Acta Biomater. 8 (2012) 20–30. doi:10.1016/j.actbio.2011.10.016.

[13] N.T. Kirkland, J. Lespagnol, N. Birbilis, M.P. Staiger, A survey of bio-corrosion rates of magnesium alloys, Corros. Sci. 52 (2010) 287–291. doi:10.1016/j.corsci.2009.09.033.

[14] X.-B. Chen, N. Birbilis, T.B. Abbott, A simple route towards a hydroxyapatite–Mg(OH)2 conversion coating for magnesium, Corros. Sci. 53 (2011) 2263–2268. doi:10.1016/j.corsci.2011.03.008.

[15] E. Zhang, D. Yin, L. Xu, L. Yang, K. Yang, Microstructure, mechanical and corrosion properties and biocompatibility of Mg-Zn-Mn alloys for biomedical application, Mater. Sci. Eng. C. 29 (2009) 987–993. doi:10.1016/j.msec.2008.08.024.

[16] J. Vormann, Magnesium: nutrition and metabolism, Mol. Aspects Med. 24 (2003) 27–37. doi:10.1016/S0098-2997(02)00089-4.

[17] R.K. Rude, Magnesium deficiency: A cause of heterogenous disease in humans, J. Bone Miner. Res. 13 (1998) 749–758. doi:10.1359/jbmr.1998.13.4.749.

[18] D. Williams, New interests in magnesium, Med Device Technol. 17 (2006) 9–10.

[19] X.B. Chen, D.R. Nisbet, R.W. Li, P.N. Smith, T.B. Abbott, M.A. Easton, D.H. Zhang, N. Birbilis, Controlling initial biodegradation of magnesium by a biocompatible strontium phosphate conversion coating, Acta Biomater. 10 (2014) 1463–1474. doi:10.1016/j.actbio.2013.11.016.

[20] F. Witte, V. Kaese, H. Haferkamp, E. Switzer, A. Meyer-Lindenberg, C.J. Wirth, H. Windhagen, In vivo corrosion of four magnesium alloys and the associated bone response, Biomaterials. 26 (2005) 3557–3563. doi:10.1016/j.biomaterials.2004.09.049.

[21] A. Krause, N. Von Der Höh, D. Bormann, C. Krause, F.W. Bach, H. Windhagen, A. Meyer-Lindenberg, Degradation behaviour and mechanical properties of magnesium implants in rabbit tibiae, J. Mater. Sci. 45 (2010) 624–632. doi:10.1007/s10853-009-3936-3.

[22] X. Zhao, L.L. Shi, J. Xu, Mg-Zn-Y alloys with long-period stacking ordered structure: In vitro assessments of biodegradation behavior, Mater. Sci. Eng. C. 33 (2013) 3627–3637. doi:10.1016/j.msec.2013.04.051.

[23] L.-Y. Li, L.-Y. Cui, R.-C. Zeng, S.-Q. Li, X.-B. Chen, Y. Zheng, M.B. Kannan, Advances in functionalized polymer coatings on biodegradable magnesium alloys - A review, Acta Biomater. (2018). doi:10.1016/J.ACTBIO.2018.08.030.

[24] J. Zhang, W. Zhang, C. Yan, K. Du, F. Wang, Corrosion behaviors of Zn/Al-Mn alloy composite coatings deposited on magnesium alloy AZ31B (Mg-Al-Zn), Electrochim. Acta. 55 (2009) 560–571. doi:10.1016/j.electacta.2009.09.026.

[25] J. Yang, F. Cui, I.S. Lee, Surface modifications of magnesium alloys for biomedical applications, Ann. Biomed. Eng. 39 (2011) 1857–1871. doi:10.1007/s10439-011-0300-y.

[26] H. Huo, Y. Li, F. Wang, Corrosion of AZ91D magnesium alloy with a chemical conversion coating and electroless nickel layer, Corros. Sci. 46 (2004) 1467–1477. doi:10.1016/j.corsci.2003.09.023.

[27] K.Y. Chiu, M.H. Wong, F.T. Cheng, H.C. Man, Characterization and corrosion studies of fluoride conversion coating on degradable Mg implants, Surf. Coatings Technol. 202 (2007) 590–598. doi:10.1016/j.surfcoat.2007.06.035.

[28] C.D. Gu, W. Yan, J.L. Zhang, J.P. Tu, Corrosion resistance of AZ31B magnesium alloy with a conversion coating produced from a choline chloride—Urea based deep eutectic solvent, Corros. Sci. 106 (2016) 108–116. doi:10.1016/j.corsci.2016.01.030.

[29] L. Guo, C. Gu, J. Zhang, X. Wang, K. Wang, Y. Jin, J. Tu, A black conversion coating produced by hot corrosion of magnesium with deep eutectic solvent membrane, Surf. Coat. Technol. (2019). doi:10.1016/j.surfcoat.2018.10.062.

[30] X. jun Cui, X. zhou Lin, C. hai Liu, R. song Yang, X. wen Zheng, M. Gong, Fabrication and corrosion resistance of a hydrophobic micro-arc oxidation coating on AZ31 Mg alloy, Corros. Sci. 90 (2015) 402–412. doi:10.1016/j.corsci.2014.10.041.

[31] H. Duan, K. Du, C. Yan, F. Wang, Electrochemical corrosion behavior of composite coatings of sealed MAO film on magnesium alloy AZ91D, Electrochim. Acta. 51 (2006) 2898–2908. doi:10.1016/j.electacta.2005.08.026.

[32] A.L.K. Tan, A.M. Soutar, I.F. Annergren, Y.N. Liu, Multilayer sol-gel coatings for corrosion protection of magnesium, Surf. Coatings Technol. 198 (2005) 478–482. doi:10.1016/j.surfcoat.2004.10.066.

[33] F. Hollstein, R. Wiedemann, J. Scholz, Characteristics of PVD-coatings on AZ31hp magnesium alloys, Surf. Coatings Technol. 162 (2003) 261–268. doi:10.1016/S0257-8972(02)00671-0.

[34] G. Wu, X. Zeng, G. Yuan, Growth and corrosion of aluminum PVD-coating on AZ31 magnesium alloy, Mater. Lett. 62 (2008) 4325–4327. doi:10.1016/j.matlet.2008.07.014.

[35] C. Christoglou, N. Voudouris, G.N. Angelopoulos, M. Pant, W. Dahl, Deposition of aluminium on magnesium by a CVD process, Surf. Coatings Technol. 184 (2004) 149–155. doi:10.1016/j.surfcoat.2003.10.065.

[36] Y. Su, Y. Su, Y. Lu, J. Lian, G. Li, Composite Microstructure and Formation Mechanism of Calcium Phosphate Conversion Coating on Magnesium Alloy, J. Electrochem. Soc. 163 (2016) G138--G143. doi:10.1149/2.0801609jes.

[37] L. Xu, F. Pan, G. Yu, L. Yang, E. Zhang, K. Yang, In vitro and in vivo evaluation of the surface bioactivity of a calcium phosphate coated magnesium alloy, Biomaterials. 30 (2009) 1512–1523. doi:10.1016/j.biomaterials.2008.12.001.

[38] R. Zeng, Z. Lan, L. Kong, Y. Huang, H. Cui, Characterization of calcium-modified zinc phosphate conversion coatings and their influences on corrosion resistance of AZ31 alloy, Surf. Coatings Technol. 205 (2011) 3347–3355. doi:10.1016/j.surfcoat.2010.11.027.

[39] L.Y. Niu, Z.H. Jiang, G.Y. Li, C.D. Gu, J.S. Lian, A study and application of zinc phosphate coating on AZ91D magnesium alloy, Surf. Coatings Technol. 200 (2006) 3021–3026. doi:10.1016/j.surfcoat.2004.10.119.

[40] X.B. Chen, X. Zhou, T.B. Abbott, M.A. Easton, N. Birbilis, Double-layered manganese phosphate conversion coating on magnesium alloy AZ91D: Insights into

coating formation, growth and corrosion resistance, Surf. Coatings Technol. 217 (2013) 147–155. doi:10.1016/j.surfcoat.2012.12.005.

[41] T. Ishizaki, I. Shigematsu, N. Saito, Surface & Coatings Technology Anticorrosive magnesium phosphate coating on AZ31 magnesium alloy, guo 203 (2009) 2288–2291. doi:10.1016/j.surfcoat.2009.02.026.

[42] N. Van Phuong, M. Gupta, S. Moon, Enhanced corrosion performance of magnesium phosphate conversion coating on AZ31 magnesium alloy, 27 (2017) 1087–1095. doi:10.1016/S1003-6326(17)60127-4.

[43] G. Duan, L. Yang, S. Liao, C. Zhang, X. Lu, Y. Yang, B. Zhang, Y. Wei, T. Zhang, B. Yu, X. Zhang, F. Wang, Designing for the chemical conversion coating with high corrosion resistance and low electrical contact resistance on AZ91D magnesium alloy, Corros. Sci. 135 (2018) 197–206. doi:https://doi.org/10.1016/j.corsci.2018.02.051.

[44] X.B. Chen, N. Birbilis, T.B. Abbott, Effect of [Ca 2+] and [PO43-] levels on the formation of calcium phosphate conversion coatings on die-cast magnesium alloy AZ91D, Corros. Sci. 55 (2012) 226–232. doi:10.1016/j.corsci.2011.10.022.

[45] Y. Su, Y. Guo, Z. Huang, Z. Zhang, G. Li, J. Lian, L. Ren, Preparation and corrosion behaviors of calcium phosphate conversion coating on magnesium alloy, Surf. Coatings Technol. 307 (2016) 99–108. doi:10.1016/j.surfcoat.2016.08.065.

[46] J.H. Hanks, Hanks' balanced salt solution and pH control - Springer, Methods Cell Sci. (1975). http://www.springerlink.com/index/P214662317R6810J.pdf.

[47] T. Ishizaki, R. Kudo, T. Omi, K. Teshima, T. Sonoda, I. Shigematsu, M. Sakamoto, Corrosion resistance of multilayered magnesium phosphate/magnesium hydroxide film formed on magnesium alloy using steam-curing assisted chemical

conversion method, Electrochim. Acta. 62 (2012) 19–29. doi:https://doi.org/10.1016/j.electacta.2011.11.034.

[48] L. Wu, L. Zhao, J. Dong, W. Ke, N. Chen, Potentiostatic Conversion of Phosphate Mineral Coating on AZ31 Magnesium Alloy in 0.1MK2HPO4 Solution, Electrochim. Acta. 145 (2014) 71–80. doi:https://doi.org/10.1016/j.electacta.2014.08.100.

[49] Z.J. Jia, M. Li, Q. Liu, X.C. Xu, Y. Cheng, Y.F. Zheng, T.F. Xi, S.C. Wei, Micro-arc oxidization of a novel Mg–1Ca alloy in three alkaline KF electrolytes: Corrosion resistance and cytotoxicity, Appl. Surf. Sci. 292 (2014) 1030–1039. doi:https://doi.org/10.1016/j.apsusc.2013.11.038.

[50] X. Zhu, Y. Liu, F. Qian, H. Shang, X. Wei, S. Zhang, J. Chen, Z.J. Ren, Carbon transmission of CO2activated nano-MgO carbon composites enhances phosphate immobilization, J. Mater. Chem. A. 6 (2018) 3705–3713. doi:10.1039/c7ta10405g.

[51] G. Duan, L. Yang, S. Liao, C. Zhang, X. Lu, Y. Yang, B. Zhang, Y. Wei, T. Zhang, B. Yu, X. Zhang, F. Wang, Designing for the chemical conversion coating with high corrosion resistance and low electrical contact resistance on AZ91D magnesium alloy, Corros. Sci. 135 (2018). doi:10.1016/j.corsci.2018.02.051.

[52] B. Wang, D. Xu, J. Dong, W. Ke, Effect of Texture on Biodegradable Behavior of an As-Extruded Mg–3%Al–1%Zn Alloy in Phosphate Buffer Saline Medium, J. Mater. Sci. Technol. 32 (2016) 646–652. doi:10.1016/j.jmst.2016.02.002.

[53] J. Chen, X. Lan, C. Wang, Q. Zhang, The formation mechanism and corrosion resistance of a composite phosphate conversion film on AM60 alloy, Materials (Basel). 11 (2018). doi:10.3390/ma11030402.

[54] S. Feliu, A. Pardo, M.C. Merino, A.E. Coy, F. Viejo, R. Arrabal, Correlation between the surface chemistry and the atmospheric corrosion of AZ31, AZ80 and AZ91D magnesium alloys, Appl. Surf. Sci. 255 (2009) 4102–4108. doi:https://doi.org/10.1016/j.apsusc.2008.10.095.

[55] P. Hollins, Impedance spectroscopy: Emphasizing solid materials and systems, Spectrochim. Acta Part A Mol. Spectrosc. (2002). doi:10.1016/0584-8539(88)80155-7.

[56] G.L. Song, Corrosion of magnesium alloys, 2011. doi:10.1533/9780857091413.

[57] G. Song, A. Atrens, Understanding magnesium corrosion. A framework for improved alloy performance, Adv. Eng. Mater. 5 (2003) 837–858. doi:10.1002/adem.200310405.

[58] M.C. Zhao, M. Liu, G. Song, A. Atrens, Influence of the β-phase morphology on the corrosion of the Mg alloy AZ91, Corros. Sci. 50 (2008) 1939–1953. doi:10.1016/j.corsci.2008.04.010.

[59] Y. Su, G. Li, J. Lian, A chemical conversion hydroxyapatite coating on AZ60 magnesium alloy and its electrochemical corrosion behaviour, Int. J. Electrochem. Sci. 7 (2012) 11497–11511.

Tables :

Figure captions :

Fig. 1. Predominance area diagram for the precipitation of Mg phosphates.

Fig. 2. SEM surface morphologies of coated samples prepared at 40°C, 60°C and 80°C in conversion solution with different pH values (2.5, 3.0, 3.5 and 4.0) (Scale bar is 20 μm).

Fig. 3. Cross-section morphologies of coated samples (Scale bar is 100 μm.)

Fig. 4. EDS results and corresponding tested area of coated samples: (a) 40°C-pH 2.5, (b) 40°C-pH 3.0, (c) 40°C-pH 3.5 and (d) 40°C-pH 4.0. (Scale bar is 40μm.)

Fig. 5. The XRD patterns of substrate Mg alloy and conversion coatings prepared at 40°C.

Fig. 6. XPS spectra of conversion coating on AZ31 Mg alloys (a) Survey XPS spectrum and high-resolution spectra of (b) P2p (c) Mg1s (d)O1s

Fig. 7. OCP curves of bare and coated samples prepared at (a) 40°C (b) 60°C and (c) 80°C.

Fig. 8. Nyquist plots of coated samples prepared at (a) 40°C (b) 60°C (c) 80°C and (d) AZ31 Mg alloy

Fig. 9. Bode plots of coated samples prepared at (a) 40°C (b) 60°C (c) 80°C and AZ31 Mg alloy.

Fig. 10. EEC models of (a) AZ31 Mg alloy and (b) coated samples in Hanks' solution.

Fig. 11. Resistances comparison (R_{out}, R_{in}, R_{ct} and R_p) from EIS fitting results (Table 3) of coated samples prepared at (a) 40°C, (b) 60°C (c) 80°C and (d) comparison of R_p of all coated samples.

Fig. 12. PDP curves of coated samples prepared at (a) 40°C, (b) 60°C, (c) 80°C and AZ31 Mg alloy in Hanks' solution at 37°C and pH 7.4 and (d) corrosion current density at different combinations of preparation temperature and pH values.

Fig. 13. Corrosion morphologies of all coated samples after the 5-day immersion test in Hanks' solution at 37°C and pH 7.4.

Fig. 14. Hydrogen evolution volume of AZ31 Mg alloy and coated samples prepared at (a) 40°C (b) 60°C and (c) 80°C tested in Hanks' solution at 37°C and pH 7.4.

Fig. 15. Schematic presentation of the formation mechanism of conversion coating.

Fig. 16. (a) Feature of conversion coating (prepared at 80°C-pH3.0) which consists of the outer layer and inner layer (b) schematic diagram of the formation of conversion coating.

Fig. 17. (a) Polarization diagram and schematic diagrams of corrosion process in (b) AZ31 Mg alloy corresponding to that two solid lines in polarization diagram, (c) coated samples prepared at low temperature (40°C) corresponding to that two dashed lines in polarization diagram and (d) coated samples prepared at high temperature (60°C and 80°C) corresponding to that two dotted lines in polarization diagram.